

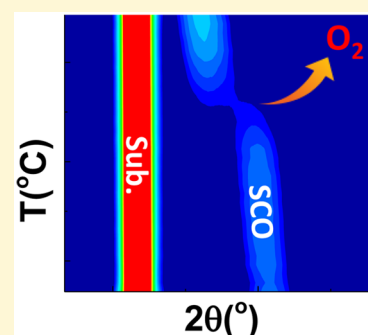
Strain-Enhanced Oxygen Dynamics and Redox Reversibility in Topotactic SrCoO_{3-δ} (0 < δ ≤ 0.5)

Songbai Hu,[†] Yu Wang,[‡] Claudio Cazorla,^{†,§} and Jan Seidel^{*,†}

[†]School of Materials Science and Engineering, [‡]Solid State and Elemental Analysis Unit, Mark Wainwright Analytical Centre, and [§]Integrated Materials Design Centre, UNSW Australia, Sydney New South Wales 2052, Australia

S Supporting Information

ABSTRACT: Oxide materials facilitating high-ion mobility and fast-ion transport are highly sought after for applications requiring intensive redox cycling. Some of these materials, in addition, may exhibit interesting multifunctional properties originating from electron correlation such as magnetism and metal–insulator transitions. SrCoO_{3-δ} (SCO) is one such compound, which recently has attracted a lot of interest due to its ability of taking on and releasing oxygen fluently. Here we investigate thoroughly the dynamics of oxygen vacancies and redox cycles in SCO under broad epitaxial strain conditions (−1.2% ≤ η ≤ +3.9%). We show that the capacity of this material to act as an “oxygen sponge” depends strongly on the strain conditions, with moderate strains of ca. +2% providing the optimal conditions for reversible redox cycling. First-principles simulation methods are employed to understand the experimental trends observed for SCO reduction in vacuum, and to provide microscopic insight into the formation of oxygen vacancies. Our work demonstrates that strain engineering can serve as an efficient means to control the dynamics of oxygen anions and redox reversibility in topotactic materials.



1. INTRODUCTION

SrCoO_{3-δ} (SCO) is a ferromagnetic metallic compound that undergoes intriguing structural, electronic, and magnetic order phase transitions as its content of oxygen is varied.^{1–7} In stoichiometric samples (δ = 0.0) SCO adopts a perovskite cubic structure (P-SCO, *a* = 3.836 Å²) that exhibits ferromagnetic spin order at temperatures below 305 K; in nonstoichiometric samples with high oxygen deficiency (δ = 0.5) SCO adopts a brownmillerite phase (BM-SCO, pseudotetragonal, *a* = *b* = 3.905 Å, *c* = 3.936 Å⁸) that exhibits atomically ordered one-dimensional vacancy channels and antiferromagnetic spin order at *T* < 570 K. Such an extraordinary dependence of functionality on oxygen stoichiometry converts SCO into an excellent material to develop new information storage and energy conversion technologies. For instance, SCO can be used as an electrode in complex oxide heterostructures thanks to its high electrical conductivity and convenient lattice parameter.⁹ SCO-based solid-solutions also can be exploited in solid oxide fuel and electrolysis cells (SOFCs/SOECs) due to their inherently high oxygen mobility and appropriate structural and electronic properties.^{10–14}

Recently, it has been shown that strain engineering can be used to efficiently control the content of oxygen in SCO thin films and hence to manipulate its functionality.^{14–18} For example, upon application of a moderate tensile epitaxial strain of ca. +2% the oxygen activation energy barrier is reduced by ca. 30%,¹⁵ which makes it possible to stabilize oxygen-deficient samples even at low annealing temperatures (~300 °C) and highly oxidizing conditions. These new findings open a promising path for the realization of low-temperature

SOFCs/SOECs.¹⁴ Nevertheless, there are still a series of fundamental questions that need to be addressed for the development of successful SCO-based technologies. First, spontaneous reduction occurs in SCO at ambient conditions,¹⁹ which is not desirable from an application perspective; whether epitaxial strain could have a blocking or a further accelerating effect on such an unwanted deterioration is yet unknown. Second, the dynamics and reversibility features of SCO redox reactions have been investigated only in a very reduced span of epitaxial strain conditions;^{14,16} whether the same kind of fast and highly reversible redox reactions that have been observed in moderately tensile strained thin films may occur also at other epitaxial strains remains to be demonstrated. Therefore, to unravel the effects of epitaxial strain on oxygen stability and to investigate nonequilibrium facets of redox reactions is critical for anticipating the likely technological challenges involving SCO thin films.

In this article, we report that both moderate compressive (ca. −1.2%) and large tensile (ca. +3.9%) epitaxial strains can reduce significantly the oxygen vacancy activation energy barrier in SCO, leading to extremely low topotactic critical temperatures in vacuum of just ca. 120–260 °C. Meanwhile, we show that the stability of oxygen content and reversibility of redox reactions depend strongly on the epitaxial strain conditions. In particular, the spontaneous sample degradation and temperature shift accompanying a reduction–oxidation

Received: October 14, 2016

Revised: December 12, 2016

Published: December 12, 2016

Table 1. Calculated in-Plane Strain between Cubic SCO and Different Substrates

material	<i>a</i> (Å)	<i>b</i> (Å)	<i>c</i> (Å)	crystal	orientation	pseudocubic <i>a_t</i> (Å)	strain (%)
SmScO ₃	5.531	5.758	7.975	orth	110	3.992	+3.9
DyScO ₃	5.44	5.71	7.89	orth	110	3.943	+2.7
SrTiO ₃	3.905	3.905	3.905	cubic	100	3.905	+1.8
LaAlO ₃	3.779	3.779	3.779	cubic	100	3.779	-1.2

cycle turn out to be minimal at a moderate tensile strain of ca. +2%. The reported strain-mediated oxygen mobility and redox reversibility in SCO thin films demonstrates a new multifaceted control of perovskite-based functionality, which shows promise for nanoelectronics and nanoionics applications.

2. EXPERIMENTAL AND THEORETICAL METHODS

A Pascal pulsed laser deposition (PLD) system with a 248 nm wavelength KrF excimer laser was used for the growth of SCO. Fully strained BM- and P-SCO thin films were grown on (100) LaAlO₃ (LAO), (100) SrTiO₃ (STO), (110) DyScO₃ (DSO), and (110) SmScO₃ (SSO) substrates. Substrates (SurfaceNet, GmbH) of different lattice constants were selected to achieve appropriate strains. 1 gives the lattice parameters of these substrates and their in-plane strains with the cubic SCO (*a* = 3.836 Å).

We started growing SCO on STO substrates considering the strain is not too high (+1.8%). Substrates had a surface orientation parallel to (001) plane with a small miscut angle of 0.1 degree. Thirty minutes of annealing in 100 mTorr of oxygen was carried out to get clean surfaces and clear terraces. For a 5 × 5 mm² substrate, the optimized conditions for our growth were substrate temperature 750 °C, oxygen pressure 100 mTorr, laser energy 150–200 mJ, laser frequency 1 Hz. After 600 pulses the thickness of the film was estimated to be 20 nm through X-ray reflectometry measurements. For the growth of BM phase, the temperature was directly dropped down to room temperature (RT) in 100 mTorr of oxygen after growth. For the growth of P phase, a following 30 min in situ annealing at 600 °C (without cooling down to RT) in 600 Torr of oxygen was carried out.

The growth of SCO thin films on the DSO substrates is a bit more difficult compared with that on STO. Note that the strain between SCO and DSO is +2.7% which is much larger than that of STO; therefore in P phase growth we have to increase the depositing and annealing temperature to get it fully strained. The optimized conditions were a substrate temperature of 800 °C, oxygen pressure of 100 mTorr, laser energy of 200 mJ, frequency of 1 Hz, and 300 laser pulses, following 30 min of in situ annealing at 700 °C in 600 Torr of oxygen. The resulting thin films were approximately 20 nm thick. For the BM phase we simply do not do post-annealing but allow cool down to room temperature directly at the rate of 30 °C/min without changing the pressure.

As the SCO thin films were grown successfully with tensile strains, we switched to the growth on (001) LAO substrate which exerts -1.2% compressive strain. The preparation of SCO on LAO substrates was an arduous work due to a narrow growth window. To make it easier, we tried to grow the BM phase first as it does not require high oxygen pressure post-annealing. The optimized conditions for the BM phase were a substrate temperature of 600 °C, oxygen pressure of 50 mTorr, laser energy of 150 mJ, frequency of 1 Hz and 1200 pulses (yields a 20 nm thick thin film), and then cooling down to RT in 100 mTorr of oxygen. However, the direct in situ growth of the P phase, that is, annealing in high oxygen pressure and temperature, was not successful. To get a P-SCO of a smooth surface, thin films of BM phase were oxidized by 10% NaClO solution for 10 min. The resulting sample was cleaned ultrasonically twice with deionized water for 5 min, and then dried in air.

The SSO substrate was put to the end due to its large strain (+3.9%) with SCO. The optimized growth conditions for the BM phase were a substrate temperature of 800 °C, oxygen pressure of 100 mTorr, laser energy of 150–200 mJ, frequency of 1 Hz, and 300 laser pulses, and then cooling down to RT in 100 mTorr of oxygen. Typical

thicknesses of the resulting thin films are ~20 nm. The P-SCO thin films were obtained by doing a 30 min in situ annealing at 700 °C in 650 Torr of oxygen.

The behavior of oxygen vacancies in SCO was studied by monitoring the redox reactions in situ using X-ray diffraction (XRD) in a wide range of epitaxial strains, that is, -1.2% to +3.9%, as a function of temperature, oxygen concentration, and time. The degradation of P-SCO on different substrates at room temperature was investigated over time at ambient conditions (air, RH = 30%) by doing XRD θ - 2θ scans (Bruker MRD, 2-bounce monochromator, 45 kV, 40 mA, λ = 1.5406 Å). The oxidation of BM-SCO at room temperature (23 °C) was realized by oxidizing with NaClO solutions of different concentration from 0.001% to 3.125%. NaClO is a strong oxidant which has the ability of oxidizing the BM-SCO to P-SCO completely.^{7,20} Immersing a BM-SCO phase sample into an aqueous NaClO oxidizing solution for a certain amount of time can yield increased oxygen contents and eventually trigger the transition to the P phase. This approach makes the phase transition happen in a straightforward way, and no special and complicated experimental setup is needed. The sample was cleaned with deionized water after 1 min of oxidizing and dried in air quickly within 1 min. The BM → P phase transitions were captured by XRD θ - 2θ scans. Each scan took 30–40 min. The redox reactions at high temperature were carried out in different environments. The P-SCO thin films were heated with a domed hot stage (Anton Paar, DHS 1100) which was pumped by a mechanical pump to a base pressure of 0.1 mbar (oxygen pressure 0.03 mbar) and monitored using a Bruker D8-TXS X-ray diffractometer (2-bounce monochromator, 45 kV, 100 mA, λ = 1.5406 Å). The oxidation of BM-SCO thin films was carried out in 5 bar of oxygen pressure (99.998% purity) with a reaction chamber (Anton Paar, XRK 900) and recorded using a Panalytical Empyrean (2-bounce monochromator, 45 kV, 45 mA, λ = 1.5406 Å) diffractometer. The temperature ramping rate was fixed to 30 °C/min. The (002) reflections were collected at every 5 °C. Thus, there will be an error bar of 10 °C for all the transition temperatures given below. The average time for each scan took 3 to 3.5 min.

We calculated the zero-temperature vacancy energy formation energy, E_{vac} , in SCO thin films considering epitaxial strains of $-2\% \leq \eta \leq +2\%$ ($\eta = (a - a_0)/a_0$, where a_0 is the equilibrium lattice constant and a represents the in-plane lattice parameter of SCO) with first-principles density functional theory methods (DFT). Temperature plays an important role for the stability of oxygen content in SCO thin films; thereby we considered also thermal contributions to the vacancy free-energy formation, $F_{\text{vac}}^{\text{harm}}$, through quasi-harmonic DFT calculations. Next, we provide an overview of the employed computational methods and explain the technical details in our calculations.

We used the generalized gradient approximation to DFT for zero-temperature calculations due to Perdew, Burke, and Ernzerhof (GGA-PBE),²¹ as implemented in the VASP package.^{22,23} A “Hubbard-U” scheme with $U = 6.0$ eV was employed for a better treatment of the 3d electrons of Co. We used the “projector augmented wave” method to represent the ionic cores,²⁴ considering the following electrons as valence states: Sr 4s, 4p, and 5s; Co 3p, 4s, and 3d; and O 2s and 2p. Wave functions were represented in a plane-wave basis truncated at 600 eV, and we used a 20-atoms $\sqrt{2} \times \sqrt{2} \times 2$ simulation cell that allows a reproduction of the usual ferroelectric and antiferrodistortive distortions in oxide perovskites^{25,26} (see Figure 6a). For integrations in the Brillouin zone (BZ), we employed a Γ -centered \mathbf{k} -point grid of $6 \times 6 \times 6$. Geometry relaxations were performed using a conjugate-gradient algorithm that changed the volume and shape of the unit cell (fulfilling the lattice vector constraints required in thin films), and the

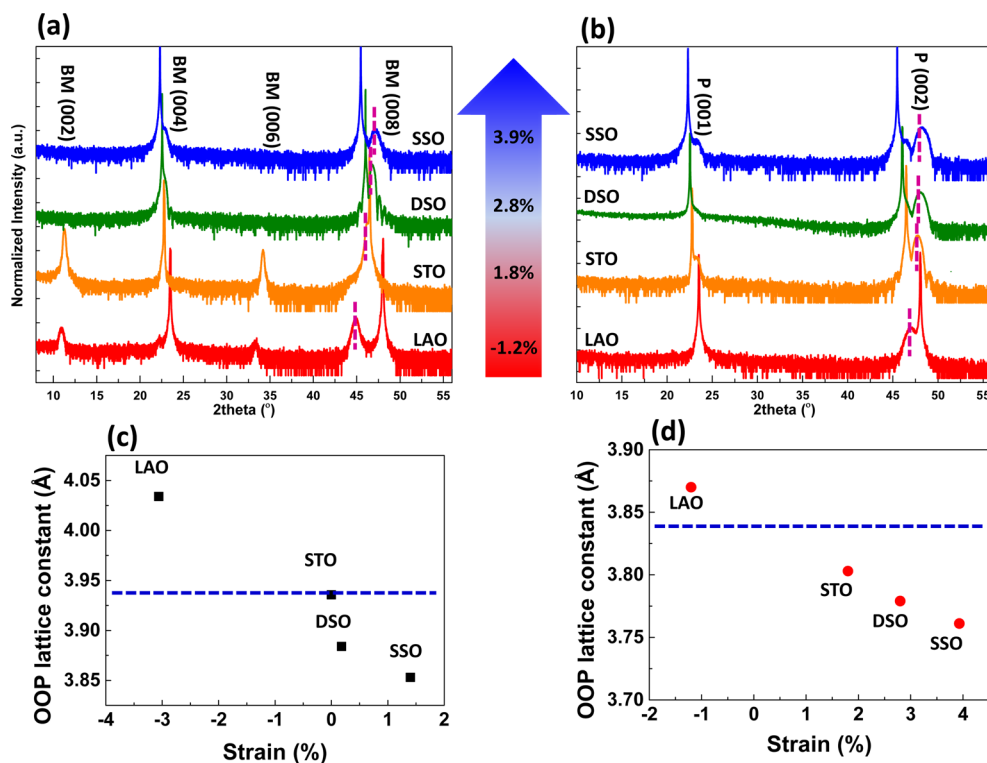


Figure 1. XRD θ - 2θ scans of as-prepared (a) BM- and (b) P-SCO thin films on different substrates. The peak positions of BM-SCO (008) and P-SCO (002) are marked with purple dashed lines. The strains between the P-SCO thin films and substrates are given in the middle. The OOP lattice constants are calculated in panels c and d for BM- and P-SCO, respectively. The blue dashed lines denote the c -lattice constants of the corresponding bulk materials.

imposed tolerance on the atomic forces was $0.01 \text{ eV}\cdot\text{\AA}^{-1}$. Using these parameters we obtained total energies that were converged to within 0.5 meV per formula unit.

We note that in order to calculate $E_{\text{vac}} = E_{\text{SrCoO}_3} - E_{\text{SrCoO}_{3-\delta}}$ we considered one oxygen vacancy, either in an apical or equatorial position, in our 20-atoms simulation cell. The computational results that we are to present, therefore, involve $\text{SrCoO}_{3-\delta}$ crystals with $\delta = 0.0$ and 0.25 , which display a P-like crystalline structure (that is, we did not simulate the orthorhombic BM phase that is stabilized at $\delta = 0.50$). In the quasi-harmonic approximation, the free-energy of a crystal is expressed as^{27,28}

$$F^{\text{harm}}(V, T) = k_{\text{B}}T \sum \ln[2 \sinh(\hbar\omega_{\text{qs}}/2k_{\text{B}}T)] \quad (1)$$

where ω_{qs} represents the square root of the eigenvalues of the dynamical force constant matrix calculated at arbitrary wave-vectors \mathbf{q} contained in the BZ, and subscript s runs over all phonon branches.²⁷ By using eq 1, we have readily estimated the thermal contribution to the vacancy free-energy formation as

$$F_{\text{vac}}^{\text{harm}}(V, T) = F_{\text{SrCoO}_3}^{\text{harm}}(V, T) - F_{\text{SrCoO}_{2.75}}^{\text{harm}}(V, T) \quad (2)$$

where superscripts indicate the types of considered crystal. To compute $F_{\text{vac}}^{\text{harm}}(V, T)$, therefore, one needs to perform vibrational phonon calculations in both stoichiometric and nonstoichiometric systems (for simplification purposes, we have neglected possible magnetic spin-disorder effects on the computation of vibrational lattice excitations²⁹).

In our phonon frequency calculations we employed the so-called “direct approach”,²⁷ in which the force-constant matrix of the crystal is directly calculated in real-space by considering the proportionality between the atomic displacements and forces when the former are sufficiently small (in our case this condition was satisfied with atomic displacements of 0.02 \AA). Large supercells containing 160 atoms were employed in order to guarantee that the elements of the force-constant matrix had all fallen off to negligible values at their boundaries, a

condition that follows from the use of periodic boundary conditions. We used a dense \mathbf{k} -point grid of $3 \times 3 \times 3$ for the calculation of the atomic forces with VASP. The computation of the nonlocal parts of the pseudopotential contributions was performed in reciprocal space, in order to maximize our numerical accuracy. Once the force-constant matrix was determined, we Fourier transformed it to obtain the phonon spectrum at any \mathbf{q} point contained in the BZ. This step was performed with the PHON code,²⁷ in which we exploited the translational invariance of the system (to impose that the three acoustic branches were exactly zero at the Γ point) and used central differences in the atomic forces (i. e., we considered positive and negative atomic displacements). A complete phonon calculation involved the evaluation of atomic forces in 120 (114) different stoichiometric (nonstoichiometric) configurations with the computational parameters just described. In order to compute F^{harm} , we employed a dense \mathbf{q} -point grid of $16 \times 16 \times 16$ for sampling of the BZ (see eq 1).

3. RESULTS AND DISCUSSIONS

3.1. Structures of As-Prepared SCO Thin Films. Figure 1 gives XRD θ - 2θ scans of our thin films for both BM- and P-SCO on different substrates. $\text{SrCoO}_{3-\delta}$ has two different crystal structures which depend on the oxygen content. In the oxygen deficiency range of 0.5 – 0.25 , SCO has BM structure, which is built up by the alternatively stacked octahedral and tetrahedral sublayers. Bulk BM-SCO is orthorhombic with lattice constants of $a = 5.5739 \text{ \AA}$, $b = 5.4697 \text{ \AA}$, and $c = 15.7450 \text{ \AA}$, which can be viewed as pseudotetragonal ($a_t = 3.905$ and $c_t/2 = 3.936 \text{ \AA}$).^{8,16} However, as the oxygen deficiency decreases to the range 0.25 – 0 , SCO will change to the P phase. P-SCO is constructed by stacking octahedra layer by layer. P-SCO is cubic with the a -lattice constant equal to 3.836 \AA .² The out-of-plane (OOP) lattice constants are calculated with Bragg’s law, and are shown

in Figure 1c,d. It decreases linearly with the in-plane (IP) strains for either BM- or P-SCO.

The strain states of all thin films were verified by doing X-ray reciprocal space maps (RSMs) around the (-103) or $(0-13)$ peak positions. The results are shown in Figure 2. The data of

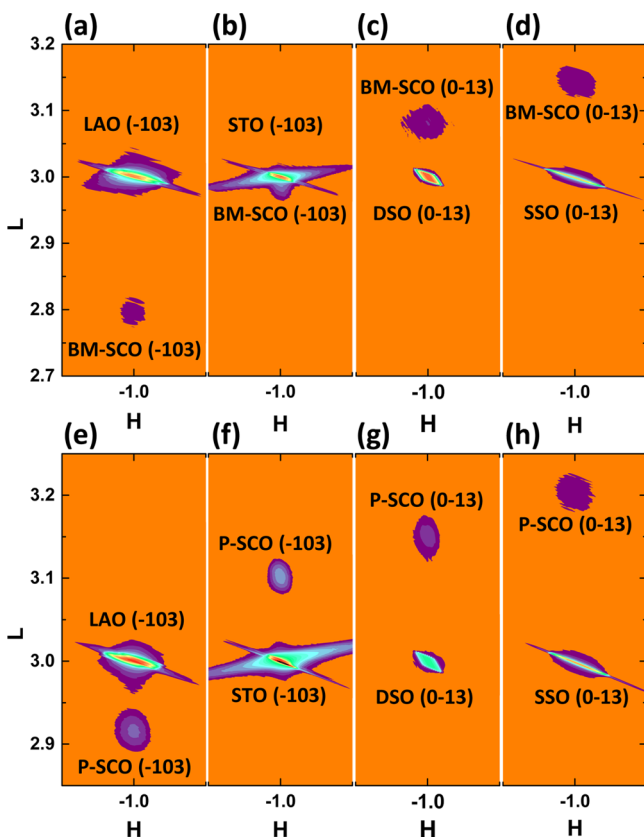


Figure 2. RSMs around the (-103) or $(0-13)$ diffractions for (a–d) BM-SCO and (e–f) P-SCO thin films grown on different substrates.

(-103) diffractions on orthorhombic DSO and SSO substrates are not shown here. The diffraction spots of either BM or P phase from the films are located at the same H positions as the substrates, indicating a coherent growth for all samples. Therefore, the in-plane lattice parameters of the films are identical to that of the substrates. The quality of the thin films under large strains is confirmed by both AFM and X-ray rocking curves, see Supplementary-2.

3.2. Oxygen Content Evolution at Room Temperature

Figure 3 gives the normalized XRD $\theta-2\theta$ scan evolution of freshly prepared P-SCO thin films on (a) LAO, (b) STO, (c) DSO, and (d) SSO substrates as a function of exposure time at ambient conditions. In Figure 3a, P-SCO on LAO degrades very quickly into a mixture of BM and P phase in 8 h after the preparation. The intensity of P-SCO peak decreases gradually with time and becomes nearly invisible after 14 days in ambient conditions; while the BM-SCO peak becomes more and more pronounced. Within 28 days P-SCO transforms into BM-SCO completely. Figure 3b shows the associated XRD peak shifts of SCO on STO substrates. No prominent change was detected even after 58 days of deposition, indicating a much higher oxygen stability as compared to that on LAO. In Figure 3c, the peak of P-SCO on DSO does not show a pronounced shift in 15 days since growth. However, it starts moving to lower angles after 29 days. The loss of oxygen with time has been confirmed with neutron diffraction.⁶ As for SCO on SSO substrate, the P-SCO peak shifts very fast to lower angles in the first 8 h, and then reduces gradually to the BM phase, see Figure 3d. In 22 days, the as-grown P-SCO converts to BM-SCO totally. The oxygen stability in SCO thin film thus shows a strong dependence on the in-plane strain conditions. Moderate tensile strains will lead to a higher oxygen stability.

Contrary to the degradation in ambient conditions, the oxidation of SCO with NaClO can oxidize the BM-SCO thin film reversibly.^{7,20} Figure 4 shows the normalized XRD $\theta-2\theta$ scan evolution of as-deposited BM-SCO thin films on (a) LAO, (b) STO, (c) DSO, and (d) SSO substrates oxidized by NaClO solution of different concentrations. In Figure 4a, the pristine BM-SCO on LAO responds retarded to the NaClO solution by looking at the $(008)_{\text{BM}}$ peak. As the concentration increases up to 0.125% mixed phases of BM and P took shape due to the intercalation of oxygen into the SCO framework. The BM phase can be diminished totally by increasing the NaClO concentration to 3.125% and pure P phase forms. A similar scenario can be seen in Figure 4b for SCO grown on the STO substrate. The only difference is that the P phase forms at the very first step of oxidizing on STO, indicating that oxygen vacancies in SCO on STO are more vulnerable to the oxidant. The oxidation of SCO on DSO is shown in Figure 4c. Different from that on LAO and STO, full oxidation of the BM into P phase occurs at the earliest stage of very low concentration (0.001%). A similar situation is observed for SCO on the SSO substrate in Figure 4d. It seems the oxidation of BM-SCO exhibits strong anisotropy along the c and a/b axis. Note that

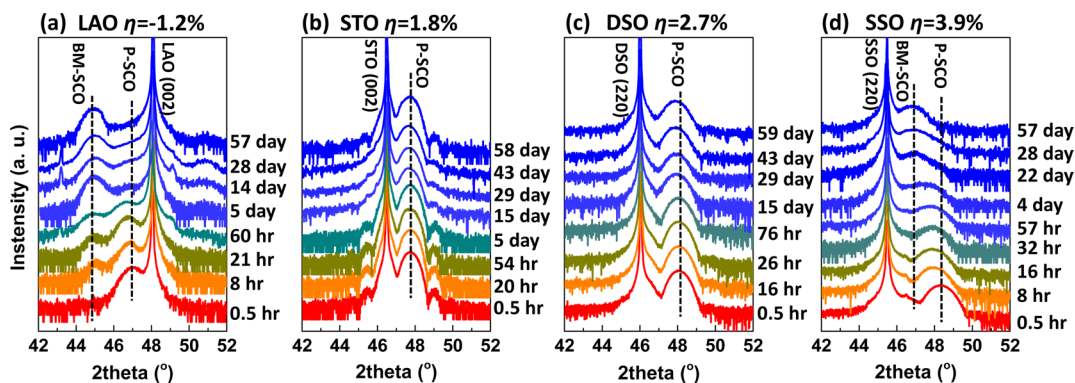


Figure 3. Normalized XRD $\theta-2\theta$ scan evolution of as-prepared P-SCO thin films on (a) LAO, (b) STO, (c) DSO, and (d) SSO substrates as a function of exposure time at ambient conditions. The black dash lines denote the peaks positions of BM-SCO (008) and P-SCO (002).

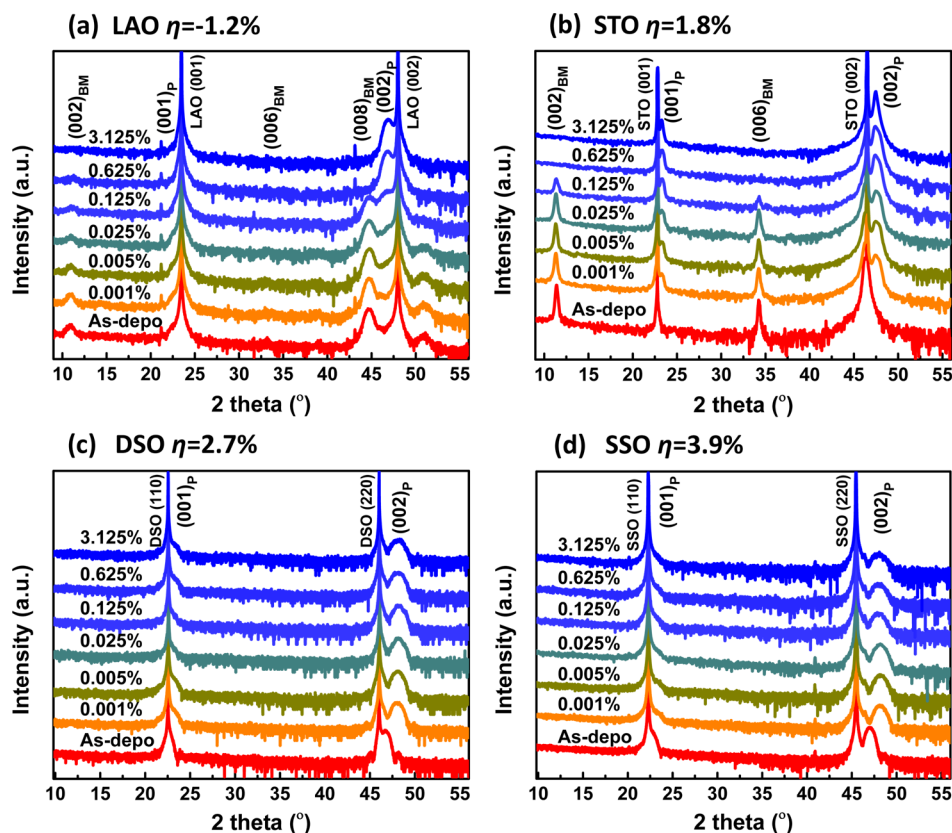


Figure 4. Normalized XRD θ - 2θ scan evolution of as-deposited BM-SCO thin films on (a) (001) LAO, (b) STO, (c) DSO, and (d) SSO substrates oxidized by NaClO solution as a function of concentrations.

the c -axis of BM-SCO on LAO and STO is normal to the sample surface, while on DSO and SSO it is parallel.

To understand this behavior we first need to look at the redox reactions happening in SCO. In the reduction process, the Co-O bond is broken by experiencing a nonstoichiometry defect reaction; then two O atoms diffuse to the surface, combine together as O_2 and volatilize into the atmosphere. As more and more O atoms are lost from the framework, P-SCO will change to BM-SCO. Note that the reduction happens spontaneously even at ambient conditions as the Gibbs energy difference between them is larger than zero.¹⁴ During the oxidation of SCO, the absorbed O on the surface will diffuse into SCO and form Co-O bonds. Many factors, such as time, thickness, temperature, oxygen pressure, oxygen diffusion energy, and oxygen vacancy formation energy, will affect the reduction and oxidation of SCO. In our experiments, the observed trends are affected by both oxygen diffusion and defect reactions as the rest of parameters remained all fixed. During oxidation, O diffusion can be treated as constant concentration diffusion. Meanwhile, in reduction, the diffusion of O from SCO to the atmosphere can be viewed as the diffusion of oxygen vacancies from vacuum to SCO. The O diffusion time in SCO can be estimated with Fick's second law:

$$C(x, t) = C_s \left[1 - \operatorname{erf} \left(\frac{x}{2\sqrt{Dt}} \right) \right] \quad (3)$$

in which $C(x, t)$ is the concentration of O (or oxygen vacancy) at thickness x and time t , C_s is the solution of O (or oxygen vacancy) at the surface layer, D is the diffusion coefficient and $\operatorname{erf}()$ is the error function. The reported D in bulk SCO

increases linearly with temperature and oxygen content.³ Taking $SCO_{2.80}$ as an example, D values at 80 °C and ~20 °C are 10^{-10} cm^2/s and 2.3×10^{-11} cm^2/s , respectively. With these values the time consumed to reach 90% and 99% of C_s after 20 nm diffusion distance is approximately 2 and 6 min, respectively, indicating an extremely fast saturation. Thus, the dominant mechanism in P-SCO reduction should be defect reactions rather than diffusion. For BM- $SCO_{2.68}$ the consumed time turns out to be 16 min and 3 h. This implies that at room temperature BM-SCO oxidation is determined by diffusion in a fast chemical treatment. However, at high temperature the defect reactions will take over again due to the sharp increase in D .

As we discussed above, the reduction of P-SCO on these four substrates is determined by the defect reactions. Using the Arrhenius equation, the concentration of oxygen vacancies can be expressed as

$$[V_{O^{\bullet\bullet}}]_R = \frac{\exp\left(-\frac{\Delta G_O}{RT}\right)}{[Co'_{Co}]^2 [O_2]^{1/2}} \quad (4)$$

$$[V'_{Co}]_O = \frac{[O_2]^{1/2} \exp\left(-\frac{\Delta G_R}{RT}\right)}{[Co^{\bullet}_{Co}]^2} \quad (5)$$

Here ΔG is the change of Gibbs free energy. The subscript "O" and "R" denotes oxidation and reduction, respectively. That means the oxygen vacancy concentration in SCO depends on the Gibbs free energy during reduction. The fast degradation of SCO on LAO and SSO indicates large ΔG_O under moderate compressive and large tensile strains; while the slow peak shift in

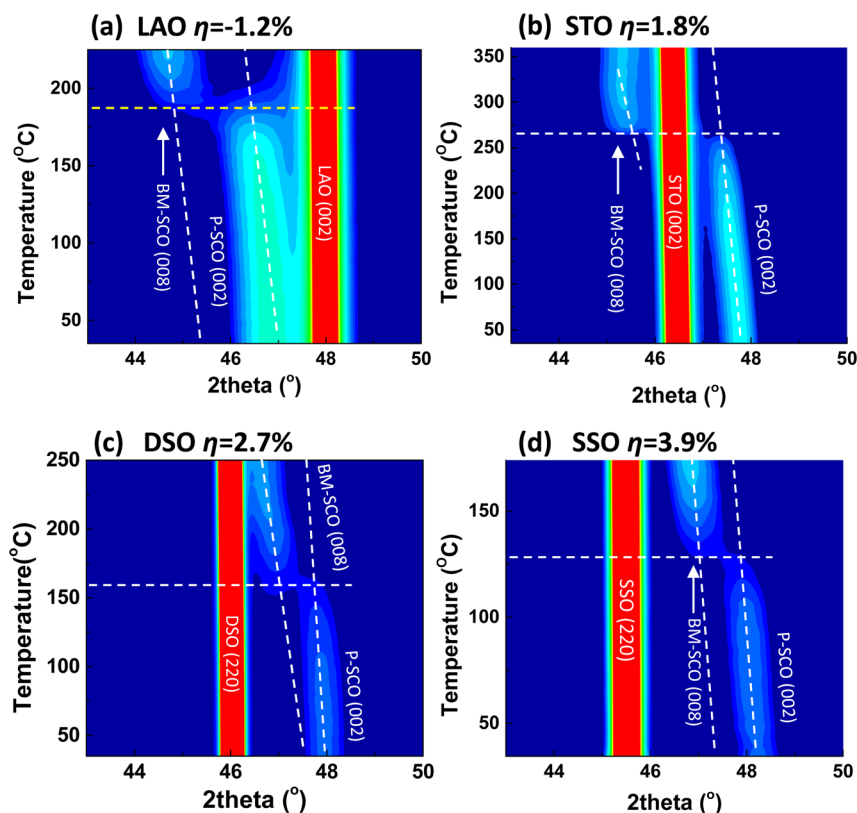


Figure 5. XRD θ - 2θ scans for P-SCO thin films on (a) LAO, (b) STO, (c) DSO, and (d) SSO substrates as a function of temperature. The SCO thin films were heated in vacuum at the rate of 30 °C/min. The white dash lines are guides to the phase transitions from the P \rightarrow BM structure.

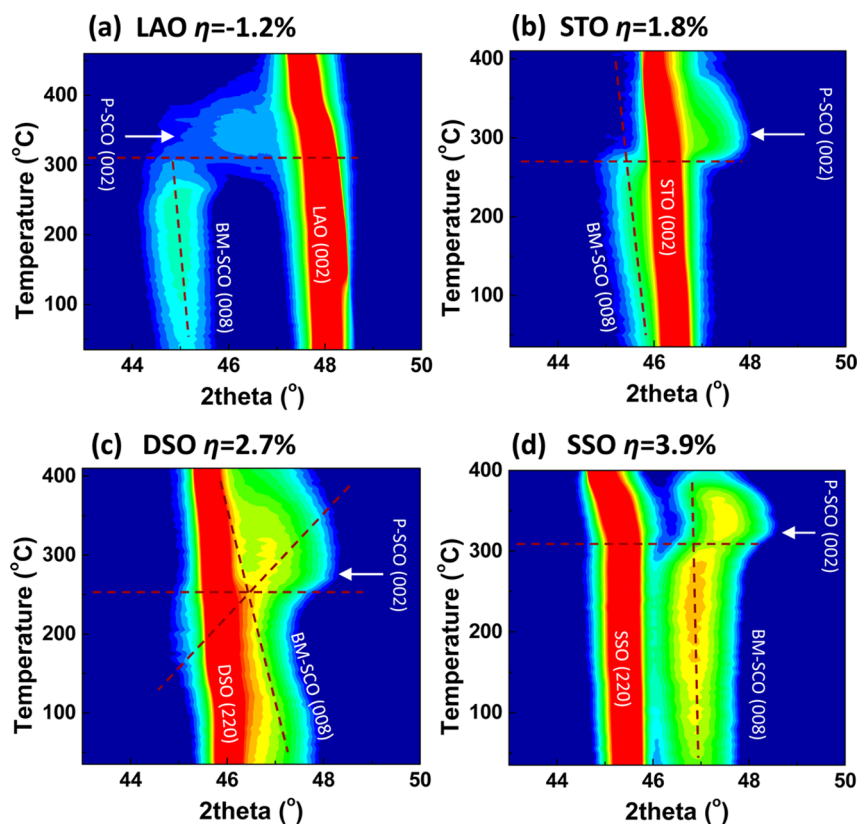


Figure 6. XRD θ - 2θ scans for P-SCO thin films on (a) LAO, (b) STO, (c) DSO, and (d) SSO substrates as a function of temperature. The SCO thin films were heated in 5 bar of oxygen at the rate of 30 °C/min.

SCO on STO and DSO implies small ΔG_O under moderate tensile strains.

However, the oxidation of BM-SCO by the fast chemical treatment was governed by the diffusion coefficient D . The above experiment indicates that oxygen diffuses extremely fast in SCO on DSO and SSO. This is probably due to the growth relations between SCO and different substrates. For BM-SCO on DSO and SSO, the tetrahedral and octahedral layers propagate in the in-plane directions, thus there are a number of oxygen vacancy openings on the surface which can speed up the diffusion significantly. Similar phenomena can be found in $\text{CaFeO}_{2.5}$.³⁰ However, for the thin films on LAO and STO substrates the number of openings is negligible as it is limited within the scale of film thickness. Thus, higher NaClO concentrations were required to increase the rate of the reaction. Therefore, the oxygen diffusivity in SCO on different substrates follows the sequence $\text{DSO} \approx \text{SSO} > \text{STO} \approx \text{LAO}$.

3.3. Oxygen Content Evolution at Elevated Temperatures.

3.3.1. Heating in Vacuum. The room-temperature experiments just discussed show that the mobility of oxygen anions can be tailored with epitaxial strain. In this section, we present analogous oxygen mobility results obtained at elevated temperatures. Figure 5 shows the XRD θ - 2θ scans for (002) reflections of P-SCO on (a) LAO, (b) STO, (c) DSO, and (d) SSO substrates as a function of temperature in vacuum. Because of the thermal expansion, the 2θ peak positions for both substrate and thin film shift to lower angles, where the P-SCO peak has a larger shift. This is due to SCO having a larger thermal expansion coefficient than the substrate on one hand;¹⁴ on the other hand, it starts to lose oxygen gradually at elevated temperatures which can increase the lattice constants as well.²⁻⁴ The evolution of the P-SCO (002) peak on LAO ($\eta = -1.2\%$) in the course of heating is given in Figure 5a. When the temperature increases to 185 °C, an immediate P \rightarrow BM phase transition occurs within 5 min. The 2θ value of 44.7° for the resulting BM phase is very close to that at room temperature (44.8°). As we increase the epitaxial strain to +1.8% at the tensile side by growing SCO on STO, the transition temperature increases up to 260 °C (Figure 5b). However, under a further increase of strain the transition temperature does not change linearly. Note that SCO on LSAT ($\eta = +0.8\%$) is reduced at 200 °C.¹⁴ The thin film on the DSO substrate ($\eta = 2.7\%$) exhibits a P \rightarrow BM phase transition at 160 °C, see Figure 5c. This down-turn trend is confirmed again by SCO on SSO ($\eta = +3.9\%$) in Figure 5d which demonstrates a phase transition at 125 °C. The reduction of P-SCO implies that the positive correlation between the oxygen stability extending from moderate compressive strain will be no longer effective at large tensile strains. This trend is consistent with the reduction at ambient conditions.

3.3.2. Heating in Oxygen. Following the reductions, we tried to oxidize BM-SCO reversibly. Figure 6 shows the XRD θ - 2θ scans for P-SCO thin films on (a) LAO, (b) STO, (c) DSO, and (d) SSO substrates as a function of temperature in 5 bar of oxygen. Similar to the heating in vacuum, the BM-SCO (008) peaks shift to lower angle as well. However, they exhibit different slopes (see dashed lines). A smaller slope implies a slower increase of out-of-plane lattice constants due to the intercalation of oxygen into the framework. As the oxygen content increases up to 2.75, the BM structure will transform into the P structure by going through a topotactic phase transition. Therefore, the BM \rightarrow P transition occurs first on DSO and then STO and LAO followed by SSO. Correspond-

ingly, the out-of-plane lattice constant decreases from 3.94 to 3.84 Å, and a peak shift can be observed simultaneously in θ - 2θ scans. In Figure 6a, the BM-SCO on LAO disappears totally at 310 °C, and a bump which represents the formation of P-SCO emerges thereafter, indicating a BM \rightarrow P phase transition during the oxidation. Due to the expansion of sample stage, the intensity of both substrate and thin film peaks will fade gradually. Thus, the bumps disappear at temperatures higher than 400 °C. Figure 6b shows the oxidizing of SCO on STO. As the epitaxial strain increases the transition temperature decreases to 270 °C. The oxidizing of BM-SCO on DSO is demonstrated in Figure 6c, in which the BM phase fades away at even low temperature (250 °C). However, on SSO substrate SCO can be oxidized only above 310 °C, see Figure 6d. The oxidizing of BM-SCO on different substrates implies that the topotactic phase transition in SCO can be effectively shaped by epitaxial strain.

The phase transition temperature as a function of strain during both procedures is plotted in Figure 7. The color bar

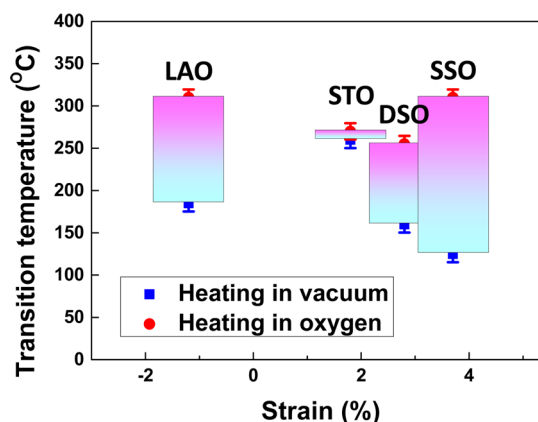


Figure 7. Phase transition temperatures of SCO thin film as a function of epitaxial strain.

between the red and blue dots denotes the hysteresis between the oxidation and reduction at the same strain. It thus reflects the reversibility of the redox reactions. We found that this gap increases significantly at lower oxygen pressure. Under an oxygen pressure of 1 bar, the BM \rightarrow P phase transition on STO ($\eta = +1.8\%$) occurs at 450 °C, which broadens the gap to 180 °C (see Supplementary-2). However, under an oxygen pressure of 5 bar the same gap is reduced to nearly zero in Figure 7. This effect can be qualitatively understood with the help of eq 4. Depending on substrates, the gap increases from 90 °C (DSO, $\eta = +2.7\%$) up to 180 °C (SSO, $\eta = +3.8\%$). That means much higher oxygen pressures are required to recover the perovskite phase on these substrates, with strains off the optimized value (ca. +1.8%) at their reduction temperature, which hinders potential applications. Even in lower oxygen pressure, that is, 1 bar, SCO on STO demonstrates a lower oxidation temperature (~ 450 °C, see supplementary) than on other substrates, for example, for YSZ ($\eta = -0.5\%$) on which SCO changes from BM to P phase at 500 °C.¹⁸ Besides the reversibility, SCO on STO exhibits the best stability among these four. It gives the highest reduction temperature of 260 °C temperature comparing with the rest, which is consistent with the reduction observed at room temperature. Therefore, SCO on STO represents a promising candidate for next generation

SOFCS which require high reversibility, stability, and low reaction temperature.

Additionally, the up-trend of transition temperature from P \rightarrow BM turns down during reduction. This behavior breaks the expectation that the transition temperature changes linearly with strain if the Gibbs free energy is considered to depend only on the unit cell volume. Other contributions, such as thermal excitations, need to be taken into account for a more satisfactory explanation. In an effort to microscopically understand the causes behind the dependence of the P to B transition temperature, T_C , on epitaxial strain (see Figure 7), we performed a comprehensive first-principles study on SCO thin films that involved intensive energy and lattice phonon DFT calculations (see section 2 for technical details). In particular, we computed the value of the (quasi-harmonic) Gibbs free energy associated with the formation of oxygen vacancies, $G_{\text{vac}}^{\text{harm}}$, as a function of epitaxial strain and temperature, (η, T) . This latter quantity can be expressed as

$$G_{\text{vac}}^{\text{harm}}[V(\eta), T] = E_{\text{vac}}[V(\eta)] + F_{\text{vac}}^{\text{harm}}[V(\eta), T] - \mu_{\text{O}}(T) \quad (6)$$

where μ_{O} represents the oxygen chemical potential, which depends on temperature and the partial oxygen pressure (assumed to be zero in the present case), and the dependence of volume on epitaxial strain is noted explicitly. $G_{\text{vac}}^{\text{harm}}$ is directly related to the reduction Gibbs free energy difference, ΔG_{R} , that has been introduced in a previous section. The first term in eq 3 represents zero-temperature (or static) contributions to the vacancy formation Gibbs free energy, whereas the second and third terms represent thermal (or dynamic) contributions to the same quantity.

It is well-known that the estimation of μ_{O} with the LDA+U and GGA+U DFT methods exhibits large errors.^{31–34} This is essentially due to a predicted overbinding of the O_2 molecule and to the technical burdens appearing in the calculation of gaseous phase enthalpies and entropies. For this reason, in addition to the limitations found in simulating large simulation cells and to the presence of large uncompensated electronic self-interaction errors,³⁴ first-principles DFT methods alone can hardly provide quantitative agreement with respect to experimentally measured reduction and oxidation temperatures in strongly correlated systems. Nevertheless, as for a fixed temperature the value of μ_{O} is independent of the epitaxial strain, we can provide theoretical arguments based on our DFT simulations that may qualitatively explain the observed $T_C(\eta)$ trends. In particular, the thermodynamically shifted Gibbs free energy of oxygen vacancy formation defined as

$$G_{\text{vac}}^{*\text{harm}}[V(\eta), T] = G_{\text{vac}}^{\text{harm}}[V(\eta), T] + \mu_{\text{O}}(T) \quad (7)$$

can be regarded as a fully meaningful quantity that provides valuable chemical insight into SCO thin films at fixed temperature.

In Figure 8b, we plot the zero-temperature vacancy formation energy, E_{vac} , calculated as a function of epitaxial strain, both for apical (Ap) and equatorial (Eq) vacancy types. E_{vac} values are negative in all the cases because at zero temperature stoichiometric thin films are always energetically more favorable than nonstoichiometric thin films. Likewise, the smaller are the $|E_{\text{vac}}|$ results, the more easily the thin film can be reduced. As it is shown in Figure 8b, creating oxygen vacancies in equatorial positions turns out to be energetically more favorable than in apical positions (that is, $|E_{\text{vac}}(\text{Eq})| < |$

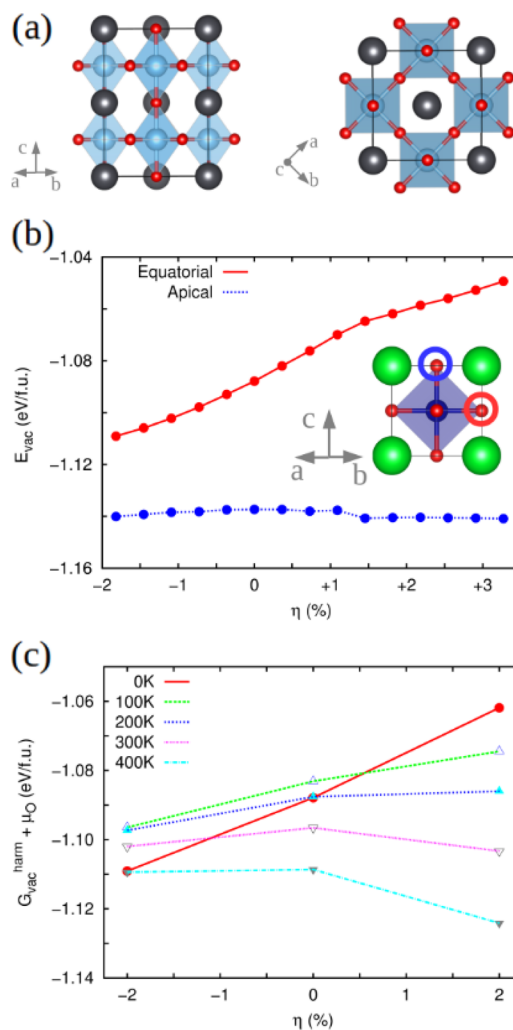


Figure 8. Details and results of our DFT calculations performed in SCO thin films; (a) Sketch of the 20-atoms simulation cell used in our E_{vac} calculations; (b) zero-temperature vacancy energy formation results expressed as a function of epitaxial strain; (c) finite temperature vacancy energy formation results expressed as a function of epitaxial strain.

$E_{\text{vac}}(\text{Ap})$); this result seems to be consistent with the structural features observed in the BM phase, which is stable at $\delta = 0.50$ and presents atomically ordered one-dimensional vacancy channels. However, by considering only static contributions to the vacancy formation energy (as it is usually done in first-principles DFT studies on oxide-based thin films, see, for instance ref 35), it is not possible to rationalize the nonlinear behavior of T_C observed in the experiments (see Figure 7, vacuum case). In particular, $E_{\text{vac}}(\text{Eq})$ increases more or less linearly with epitaxial strain, which wrongly would imply also a linear dependence of T_C on η .

In Figure 8c, we show the thermodynamically shifted Gibbs free energy associated with the formation of oxygen vacancies, $G_{\text{vac}}^{*\text{harm}}$, expressed as a function of epitaxial strain and temperature. We considered only equatorial vacancies in this case as, based on the analysis of the atomic projected density of vibrational states obtained in the stoichiometric system, we realized that both apical and equatorial vacancies contribute practically equally to $F_{\text{vac}}^{\text{harm}}$ (hence the formation of equatorial vacancies will be also preferred over that of apical vacancies when considering thermal effects). Interestingly, we found that

thermal contributions to $G_{\text{vac}}^{\text{*harm}}$ favor significantly the formation of O vacancies in thin films under compressive strains (i.e., $|G_{\text{vac}}^{\text{*harm}}|$ increases more rapidly at $\eta > 0$ conditions when T is increased). (We note that when adopting experimental values for μ_{O} —see eq 3—the resulting Gibbs free energies for oxygen vacancy formation, $G_{\text{vac}}^{\text{harm}}$ are always positive and of the order of ~ 0.1 eV/f.u., which indicates a very strong propensity toward reduction.) This tendency is contrary to the one revealed for static contributions, which clearly favors the formation of O vacancies in thin films under tensile strains (i.e., $|E_{\text{vac}}|$ decreases as η increases).

By combining the two opposed trends obtained for static- and dynamic-like contributions to $G_{\text{vac}}^{\text{*harm}}$, we can understand qualitatively the nonlinear $T_{\text{C}}(\eta)$ behavior observed in the experiments (see Figure 7, vacuum case). At large compressive strain conditions, $\eta \ll 0$, thermal contributions to $G_{\text{vac}}^{\text{*harm}}$ are dominant and strongly favor reduction; at large tensile strain conditions, $\eta \gg 0$, static contributions to $G_{\text{vac}}^{\text{*harm}}$ are dominant and also favor reduction quite significantly. In both cases, the resulting transition temperatures are small. At small epitaxial strains, however, neither the static nor the dynamic contributions to $G_{\text{vac}}^{\text{*harm}}$ are specially favorable to reduction, hence $T_{\text{C}}(\eta)$ increases as compared to the two previous cases. Therefore, the interplay between zero-temperature energy and thermal excitations to $G_{\text{vac}}^{\text{*harm}}$ appears to be crucial to understand the origins of the observed $T_{\text{C}}(\eta)$ nonlinearity.

4. CONCLUSION

We have shown that the stability and dynamics of oxygen anions in SCO thin films can be tuned by means of epitaxial strain. In particular, we have found that both moderate compressive (ca. -1.2%) and large tensile (ca. $+3.9\%$) epitaxial strains can reduce dramatically the activation energy of oxygen vacancies, leading to extremely low topotactic critical temperatures in vacuum, T_{C} , of just ca. $120\text{--}260$ °C. Also, we have shown that the variation of T_{C} induced by epitaxial strain is highly nonlinear as a result of the competition between static and thermal contributions to the formation energy of oxygen vacancies. Meanwhile, the stability of oxygen content and reversibility of redox reactions are also strongly dependent on the strain conditions. Specifically, the temperature shift accompanying a redox cycle and spontaneous degradation of SCO thin films turn out to be minimal at a moderate tensile strain of ca. $+2\%$. The reported simultaneous variation of oxygen stoichiometry, anion diffusivity, and redox reaction reversibility represents a new level of control in perovskite-based functionality achieved by strain engineering,^{36–40} which opens exciting new opportunities in the fields of nano-electronics and nanoionics.

■ ASSOCIATED CONTENT

Supporting Information

The Supporting Information is available free of charge on the ACS Publications website at DOI: [10.1021/acs.chemmater.6b04360](https://doi.org/10.1021/acs.chemmater.6b04360).

XRD $\theta\text{--}2\theta$ scans for BM-SCO thin film on STO substrate as a function of temperature; AFM surface topography of P-SCO and BM-SCO on different substrates; rocking curves of (a) P-SCO and (b) BM-SCO thin films (PDF)

■ AUTHOR INFORMATION

Corresponding Author

*E-mail: jan.seidel@unsw.edu.au.

ORCID

Jan Seidel: 0000-0003-2814-3241

Notes

The authors declare no competing financial interest.

■ ACKNOWLEDGMENTS

This research was supported through the Australian Research Council's Discovery Grants and Future Fellowship funding schemes. Computational resources and technical assistance were provided by the Australian Government through Magnus under the National Computational Merit Allocation Scheme.

■ REFERENCES

- (1) Takeda, T.; Watanabe, H.; Yamaguchi, Y. Magnetic Structure of $\text{SrCoO}_{2.5}$. *J. Phys. Soc. Jpn.* **1972**, *33*, 970–972.
- (2) Taguchi, H.; Shimada, M.; Koizumi, M. The Effect of Oxygen Vacancy on the Magnetic Properties in the System $\text{SrCoO}_{3-\delta}$ ($0 < \delta < 0.5$). *J. Solid State Chem.* **1979**, *29*, 221–225.
- (3) Takeda, Y.; Kanno, R.; Takada, T.; Yamamoto, O.; Takano, M.; Bando, Y. Phase Relation and Oxygen-non-stoichiometry of Perovskite-like Compound SrCoO_x ($2.29 < x < 2.80$). *Z. Anorg. Allg. Chem.* **1986**, *541*, 259–270.
- (4) Nemudry, A.; Rudolf, P.; Schollhorn, R. Topotactic Electrochemical Redox Reactions of the Defect Perovskite $\text{SrCoO}_{2.5+x}$. *Chem. Mater.* **1996**, *8*, 2232–2238.
- (5) Long, Y. W.; Kaneko, Y.; Ishiwata, S.; Taguchi, Y.; Tokura, Y. Synthesis of Cubic SrCoO_3 Single Crystal and Its Anisotropic Magnetic and Transport Properties. *J. Phys.: Condens. Matter* **2011**, *23*, 245601.
- (6) Callori, S. J.; Hu, S.; Bertinshaw, J.; Yue, Z. J.; Danilkin, S.; Wang, X. L.; Nagarajan, V.; Klose, F.; Seidel, J.; Ulrich, C. Strain-induced Magnetic Phase Transition in $\text{SrCoO}_{3-\delta}$ Thin Films. *Phys. Rev. B: Condens. Matter Mater. Phys.* **2015**, *91*, 140405-R.
- (7) Hu, S.; Seidel, J. Oxygen Content Modulation by Nanoscale Chemical and Electrical Patterning in Epitaxial $\text{SrCoO}_{3-\delta}$ ($0 < \delta \leq 0.5$) Thin Films. *Nanotechnology* **2016**, *27*, 325301.
- (8) Munoz, A.; de la Calle, C.; Alonso, J. A.; Botta, P. M.; Pardo, V.; Baldomir, D.; Rivas, J. Crystallographic and Magnetic Structure of $\text{SrCoO}_{2.5}$ Brownmillerite: Neutron Study Coupled with Band-Structure Calculations. *Phys. Rev. B: Condens. Matter Mater. Phys.* **2008**, *78*, 054404.
- (9) Hoffmann, M.; Borisov, V. S.; Ostanin, S.; Mertig, I.; Hergert, W.; Ernst, A. Magnetic Properties of Defect-free and Oxygen-deficient Cubic $\text{SrCoO}_{3-\delta}$. *Phys. Rev. B: Condens. Matter Mater. Phys.* **2015**, *92*, 094427.
- (10) Lee, K. T.; Wachsmann, E. D. Role of Nanostructures on SOFC Performance at Reduced Temperatures. *MRS Bull.* **2014**, *39*, 783–791.
- (11) Tsvetkov, N.; Lu, Q. Y.; Yildiz, B. Improved Electrochemical Stability at the Surface of $\text{La}_{0.8}\text{Sr}_{0.2}\text{CoO}_3$ Achieved by Surface Chemical Modification. *Faraday Discuss.* **2015**, *182*, 257–269.
- (12) Shao, Z. P.; Haile, S. M. A High-Performance Cathode for the Next Generation of Solid-Oxide Fuel Cells. *Nature* **2004**, *431*, 170–173.
- (13) Tsvetkov, N.; Lu, Q.; Sun, L.; Crumlin, E. J.; Yildiz, B. Improved Chemical and Electrochemical Stability of Perovskite Oxides with Less Reducible Cations at the Surface. *Nat. Mater.* **2016**, *15*, 1010–1016.
- (14) Jeon, H.; Choi, W. S.; Biegalski, M. D.; Folkman, C. M.; Tung, I. C.; Fong, D. D.; Freeland, J. W.; Shin, D.; Ohta, H.; Chisholm, M. F.; Lee, H. N. Reversible Redox Reactions in an Epitaxially Stabilized SrCoO_x Oxygen Sponge. *Nat. Mater.* **2013**, *12*, 1057–1063.
- (15) Petrie, J. R.; Mitra, C.; Jeon, H.; Choi, W. S.; Meyer, T. L.; Reboredo, F. A.; Freeland, J. W.; Eres, G.; Lee, H. N. Strain Control of

Oxygen Vacancies in Epitaxial Strontium Cobaltite Films. *Adv. Funct. Mater.* **2016**, *26*, 1564–1570.

(16) Jeon, H.; Choi, W. S.; Freeland, J. W.; Ohta, H.; Jung, C. U.; Lee, H. N. Topotactic Phase Transformation of the Brownmillerite $\text{SrCoO}_{2.5}$ to the Perovskite $\text{SrCoO}_{3-\delta}$. *Adv. Mater.* **2013**, *25*, 3651–3656.

(17) Hu, S.; Yue, Z.; Lim, J. S.; Callori, S. J.; Bertinshaw, J.; Ikeda-Ohno, A.; Ohkochi, T.; Yang, C. H.; Wang, X.; Ulrich, C.; Seidel, J. Growth and Properties of Fully Strained SrCoO_x ($x \approx 2.8$) Thin Films on DyScO_3 . *Adv. Mater. Interfaces* **2015**, *2*, 1500012.

(18) Lu, Q.; Yildiz, B. Voltage-Controlled Topotactic Phase Transition in Thin-Film SrCoO_x Monitored by In Situ X-ray Diffraction. *Nano Lett.* **2016**, *16*, 1186–1193.

(19) Hao, L.; Zhang, Z. F.; Xie, X. N.; Wang, H. R.; Yu, Q. X.; Zhu, H. Preparation of SrCoO_x Thin Films on LaAlO_3 Substrate and Their Reversible Redox Process at Moderate Temperatures. *J. Cryst. Growth* **2015**, *427*, 36–41.

(20) Ichikawa, N.; Iwanowska, M.; Kawai, M.; Calers, C.; Paulus, W.; Shimakawa, Y. Reduction and Oxidation of $\text{SrCoO}_{2.5}$ Thin Films at Low Temperatures. *Dalton Trans.* **2012**, *41*, 10507–10510.

(21) Perdew, J. P.; Burke, K.; Ernzerhof, M. Generalized Gradient Approximation Made Simple. *Phys. Rev. Lett.* **1996**, *77*, 3865–3868.

(22) Kresse, G.; Furthmüller, J. Efficient Iterative Schemes for Ab Initio Total-energy Calculations Using a Plane-wave Basis Set. *Phys. Rev. B: Condens. Matter Mater. Phys.* **1996**, *54*, 11169–11186.

(23) Kresse, G.; Joubert, D. From Ultrasoft Pseudopotentials to the Projector Augmented-Wave Method. *Phys. Rev. B: Condens. Matter Mater. Phys.* **1999**, *59*, 1758–1775.

(24) Blochl, P. E. Projector Augmented-wave Method. *Phys. Rev. B: Condens. Matter Mater. Phys.* **1994**, *50*, 17953–17979.

(25) Cazorla, C.; Stengel, M. Ab Initio Design of Charge-Mismatched Ferroelectric Superlattices. *Phys. Rev. B: Condens. Matter Mater. Phys.* **2014**, *90*, 020101-R.

(26) Cazorla, C.; Stengel, M. Electrostatic Engineering of Strained Ferroelectric Perovskites from First Principles. *Phys. Rev. B: Condens. Matter Mater. Phys.* **2015**, *92*, 214108.

(27) Alfe, D. PHON: A Program to Calculate Phonons Using the Small Displacement Method. *Comput. Phys. Commun.* **2009**, *180*, 2622–2633.

(28) Cazorla, C.; Errandonea, D.; Sola, E. High-pressure Phases, Vibrational Properties, and Electronic Structure of $\text{Ne}(\text{He})_2$ and $\text{Ar}(\text{He})_2$: A First-principles Study. *Phys. Rev. B: Condens. Matter Mater. Phys.* **2009**, *80*, 064105.

(29) Cazorla, C.; Iniguez, J. Insights into the Phase Diagram of Bismuth Ferrite From Quasiharmonic Free-Energy Calculations. *Phys. Rev. B: Condens. Matter Mater. Phys.* **2013**, *88*, 214430.

(30) Inoue, S.; Kawai, M.; Ichikawa, N.; Kageyama, H.; Paulus, W.; Shimakawa, Y. Anisotropic Oxygen Diffusion at Low Temperature in Perovskite-Structure Iron Oxides. *Nat. Chem.* **2010**, *2*, 213–217.

(31) Jones, R. O.; Gunnarsson, O. The Density Functional Formalism, Its Applications and Prospects. *Rev. Mod. Phys.* **1989**, *61*, 689–746.

(32) Patton, D. C.; Porezag, D. V.; Pederson, M. R. Simplified Generalized-gradient Approximation and Anharmonicity: Benchmark Calculations on Molecules. *Phys. Rev. B: Condens. Matter Mater. Phys.* **1997**, *55*, 7454–7459.

(33) Hammer, B.; Hansen, L. B.; Norskov, J. K. Improved Adsorption Energetics within Density-functional Theory Using Revised Perdew-Burke-Ernzerhof Functionals. *Phys. Rev. B: Condens. Matter Mater. Phys.* **1999**, *59*, 7413–7421.

(34) Wang, L.; Maxisch, T.; Ceder, G. Oxidation Energies of Transition Metal Oxides within the GGA+U Framework. *Phys. Rev. B: Condens. Matter Mater. Phys.* **2006**, *73*, 195107.

(35) Aschauer, U.; Pfenniger, R.; Selbach, S. M.; Grande, T.; Spaldin, N. A. Strain-controlled Oxygen Vacancy Formation and Ordering in CaMnO_3 . *Phys. Rev. B: Condens. Matter Mater. Phys.* **2013**, *88*, 054111.

(36) Seidel, J.; Luo, W.; Suresha, S. J.; Nguyen, P. K.; Lee, A. S.; Kim, S. Y.; Yang, C. H.; Pennycook, S. J.; Pantelides, S. T.; Scott, J. F.;

Ramesh, R. Prominent Electrochromism through Vacancy-order Melting in a Complex Oxide. *Nat. Commun.* **2012**, *3*, 799.

(37) Scullin, M. L.; Yu, C.; Huijben, M.; Mukerjee, S.; Seidel, J.; Zhan, Q.; Moore, J.; Majumdar, A.; Ramesh, R. Anomalous Large Measured Thermoelectric Power Factor in $\text{Sr}_{1-x}\text{La}_x\text{TiO}_3$ Thin Films Due to SrTiO_3 Substrate Reduction. *Appl. Phys. Lett.* **2008**, *92*, 202113.

(38) Lim, J. S.; Lee, J. H.; Ikeda-Ohno, A.; Ohkochi, T.; Kim, K. S.; Seidel, J.; Yang, C. H. Electric-field-induced Insulator to Coulomb Glass Transition via Oxygen-vacancy Migration in Ca-doped BiFeO_3 . *Phys. Rev. B: Condens. Matter Mater. Phys.* **2016**, *94*, 035123.

(39) Heo, Y.; Kan, D.; Shimakawa, Y.; Seidel, J. Resistive Switching Properties of Epitaxial $\text{BaTiO}_{3-\delta}$ Thin Films Tuned by After-growth Oxygen Cooling Pressure. *Phys. Chem. Chem. Phys.* **2016**, *18*, 197–204.

(40) Ikeda-Ohno, A.; Lim, J. S.; Ohkochi, T.; Yang, C. H.; Seidel, J. Investigation of Continuous Changes in the Electric-field-induced Electronic State in $\text{Bi}_{1-x}\text{Ca}_x\text{FeO}_{3-\delta}$. *Phys. Chem. Chem. Phys.* **2014**, *16*, 17412–17416.